14th International Symposium on Particle Image Velocimetry – ISPIV 2021
August 1–5, 2021

Application of Simultaneous Time-Resolved 3-D PTV and Two-colour LIF in Studying Rayleigh-Benard Convection

Sina Kashanj and David S. Nobes*

University of Alberta, Department of Mechanical Engineering, Edmonton, Canada

* dnobes@ualberta.ca

Abstract

To study the flow topology and temperature distribution of Rayleigh-Benard convection in a highly slender cell, measurement of the simultaneous velocity and temperature in the 3-D domain is required. For this aim, implementing a simultaneous time-resolved 3-D PTV and two-colour PLIF is planned. As a part of this development, for both PTV and two-colour PLIF techniques, the experimental setup has been implemented separately to measure time-resolved 2-D velocity and temperature and is presented in this paper. For PTV, a scanning system is also utilized to scan the flow field to capture the planar velocity in different depths of the flow domain. Progress on calculation of the out-of-plane velocity component including the theory is discussed. Finally, results of the time-resolved 2-D PTV and PLIF systems are presented.

1 Introduction

Buoyancy-driven flow in an enclosure heated from below and cooled from above is known as Rayleigh-Benard convection, (RBC) Adrian (2013). RBC is an idealized flow system to study the flow and heat transfer of a wide spectrum of phenomena and applications from engineering to geophysical subject matter Couston et al. (2019). Different parameters such as the temperature of the heat source and sink, working fluid and geometry of the cell can affect the convective heat transfer coefficient in RBC Zwirner et al. (2020). It is also shown that the number of large scale circulations (LSCs) which is dependent on the geometry itself can affect the heat transfer Zwirner et al. (2020).

Measuring the temperature of the flow field in RBC is crucial in experimental studies, since it is almost accepted that the kinetic and thermal energy both are added to the flow by the rise and fall of the thermal plumes Adrian (2013). There are different techniques to measure the temperature such as thermocouples, liquid crystal thermography, phosphorescent thermography, and fluorescent thermography. Planar laser-induced fluorescence (PLIF) is a non-intrusive fluorescent thermography technique that can be applied for measurement of the temperature of liquid and gaseous flow fields Sakakibara and Adrian (1999). To reduce the effect of uncertainty sources such as laser fluctuation and increase the temperature sensitivity, two-colour PLIF technique has been developed. Rhodamine B and Rhodamine 110 are a common pair of fluorescent dyes for two-colour PLIF in aqueous flow Kim and Kihm (2001), Song and Nobes (2011). It is shown that by pairing other fluorescent dyes such as Fluorescein-Rhodamine B, Fluorescein-Kiton red, and Fluorescein-Rhodamine 101 the temperature sensitivity can be enhanced up to around $\sim 7\,\%/℃$ for high temperatures (~ 50 ℃) Sutton et al. (2008). It is also shown that for low temperatures, $T < 20$ ℃ the temperature sensitivity decreases significantly Behshad et al.(2010). The highest temperature sensitivity obtained in the range of $5 < T < 20$ ℃ is around $\sim 4.2\,\%/℃$ Behshad et al.(2010).

To visualize the flow field of RBC and investigate the effect of the flow structures, measurement of the velocity of the flow field is required. Particle tracking velocimetry (PTV) which is a non-intrusive velocity measurement technique can be applied to measure the velocity with high spatial resolution Raffel et al. (2018). To capture the out of plane velocity and obtain all three velocity components, scanning

has been used with particle image velocimetry (PIV), and PTV in a variety of cases with steady or low velocity conditions such as in microfluidics (by applying confocal microscopy) Bown et al. (2007) and in natural convection studies Fujisawa et al. (2005), Kazemi et al. (2016). Since the scanning technique can be applied in cases with small geometries and can be applied simultaneously with other techniques such as PLIF, it is an advantageous technique in comparison to other 3-D velocity measurement techniques such as tomographic PIV or 3DPTV.

A simultaneous time-resolved 3-D PTV and two-colour PLIF system is under development by the authors. The aim of this paper is to investigate the approach to develop such a system to measure the velocity and temperature of a large aspect ratio square cross-section RBC cell. Furthermore, the next steps to achieve the 3-D simultaneous measurement such as the theory of calculating the out-of-plane velocity component is discussed.

2 Experimental Setup

The slender cell of the RBC with dimensions of 5×5×50 mm^3 and aspect ratio, $\Gamma = W/h$ equal to 0.1 is shown in Figure 1(a). Windows are made from acrylic sheet with a thickness of 6.35 mm that has a low thermal conduction coefficient of 0.2 W/mK. Based on the described test cell, the temperature boundary condition which is shown in Figure 1(a) can be described as a temperature constant at the top and bottom and adiabatic at the side walls. The field of view (FOV) of the imaging systems where the temperature and velocity investigation was carried out is also shown in Figure 1(a). A rendering of the physical set of the slender cell used for this experiment is shown in Figure 1(b). Two heat exchangers contain a base and a copper plate is connected to the two water baths. The base is fabricated by additive manufacturing (Form3, Formlabs Inc.) using a clear resin material with a low thermal conduction coefficient (0.15 W/mK).

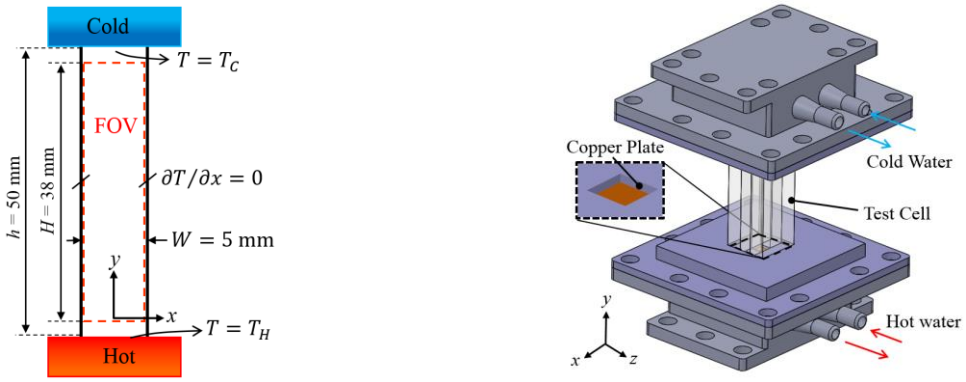

(a) (b)

Figure 1: (a) A schematic of the dimensions and boundary conditions of the test cell and (b) a rendering of the solid model of the slender rectangular RBC cell and

A schematic of the optical measurement system set to apply 3-D PTV and two-colour PLIF is shown in Figure 2(a) and (b) respectively. A diode pump laser with a maximum power of 2 W and wavelength of 532 nm was used to illuminate the seeding particles and excite the fluorescent dyes. Two scanning mirrors (ThorLabs Inc.) are used to make the laser sheet (scanning mirror-*y*) and scan the laser sheet in the depth of the channel, *z*-direction (scanning mirror-*z*). As can be observed in Figure 2(a), a double convex lens with a focal length of 80 mm after the scanning mirrors makes the laser sheet parallel to the *x*-*y* plane in each *z*. To apply 3-D PTV, an 8-bit high-speed CMOS cameras (Flare 12M125, IO Industries Inc.) with a maximum frame rate of 220 fps and resolution of 2048 pixels × 2048 pixels is utilized. The optical system used to apply two-colour PLIF, shown in Figure 2(b), is the same as the 3-D PTV optical system, but instead of one camera, two cameras, one for each colour of fluorescent dye is used with an appropriate filter used used to capture the signal of each dye separately.

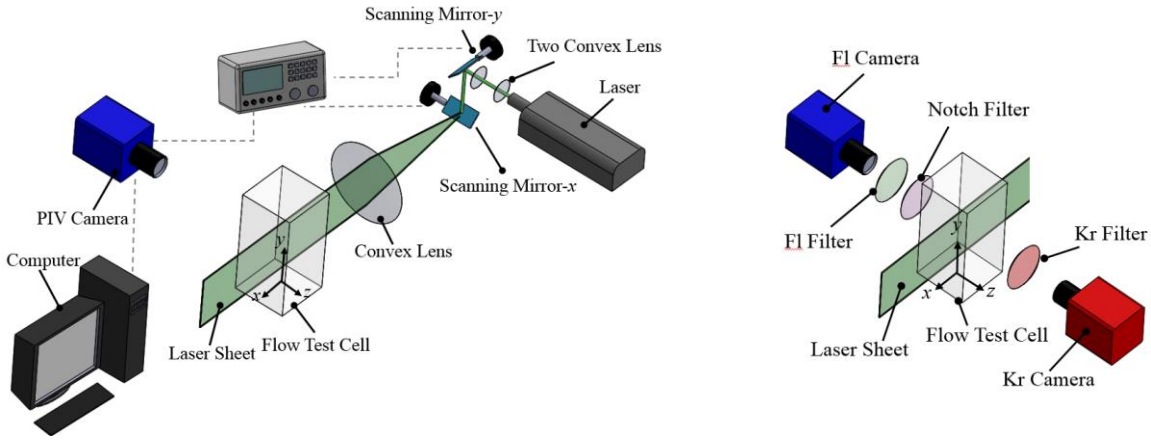

(a) (b)

Figure 2: Schematic of the optical measurement system used for (a) 3-D PTV and (b) two-colour LIF

A two-channel function generator is used to control the frequency and amplitude of the scanning mirrors. A signal generator also is utilized to synchronize the cameras and the two scanning mirrors. A timing plot of the signals generated to control the scanning mirrors and synchronize them with the cameras is illustrated in Figure 3. In this figure, signal *A* is the waveform that scan the laser sheet in depth of the test section. The initial voltage of this waveform defines the initial position of the laser sheet in the *z*-direction (by the voltage-space calibration). For this experiment 50 slices with 0.1 mm space are used to scan the depth of the channel in 12.5 s, which is significantly faster than the time scale of motion for this flow which is on the order of minutes. The laser sheet thickness is equal to ~150 mm which makes the scans with 50 % overlap. Signal *B* in Figure 3 is set to scan the laser beam in the *y*-direction to make the laser sheet. Signal *C* is a TTL signal generated to control the framerate of the cameras and synchronize the cameras with the scanning mirrors. For each plane, five TTL signals were generated to capture five frames at each plane. PTV processing is applied to each captured five frames for each plane since scanning is used only after establishment of the steady fully-developed flow.

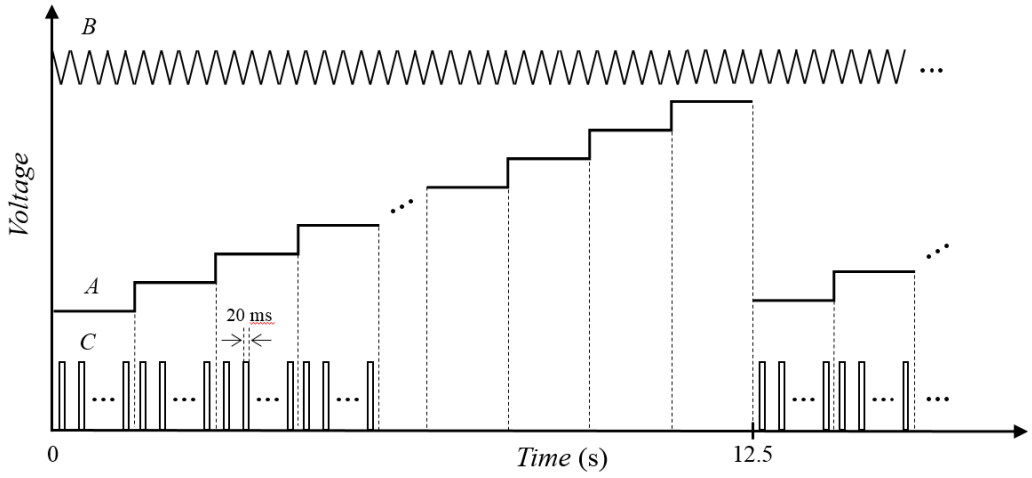

Figure 3: Schematic diagram of the three signals produced to synchronize the two scanning mirrors and the cameras.

3 Two-colour PLIF

To apply the two-colour PLIF, sodium fluorescein (Fl) and kiton red (Kr) were chosen as the fluorescent dyes. Properties of the two fluorescent dyes is shown in Table 1. A schematic of the variation of the absorption and emission spectra of the dyes with wavelength is illustrated in Figure 4 along with the location of the illumination laser at 532 nm. Though the absorption wavelength of Fl has a limited interface with the 532 nm light, it still can be excited with sufficient power. To avoid receiving the signal of the laser, a notch filter (Edmund Optics) with central wavelength (CWL) of 532 nm and full width at half maximum (FWHM) of 17 nm is utilized which is shown with light gray in Figure 4

The Fl signal (which is shown with light green in Figure 4) was collected using a bandpass filter (Edmund Optics) with CWL of 525 nm and FWHM of 50 nm. The 532 nm laser light is also used to excite Kr and the emitted signal has a maximum temperature sensitivity in the range of 560 to 620 nm Bown et al. (2007). Therefore, to capture the Kr signal with maximum temperature sensitivity and to avoid receiving the Fl emitted signal, a bandpass filter (Edmund Optics) with CWL of 607 nm and FWHM of 36 nm is used, shown in light orange in Figure 4.

Table 1: Properties of the fluorescent dyes used in two-colour LIF

Fluorescent dye	Empirical formula	Molecular weight	λ_{abs} at peak (nm)	λ_{em} at peak (nm)
Fluorescein	$C_{20}H_{10}Na_2O_5$	376.27	586	490
Kiton red	$C_{27}H_{29}N_2NaO_7S_2$	580.65	565	514

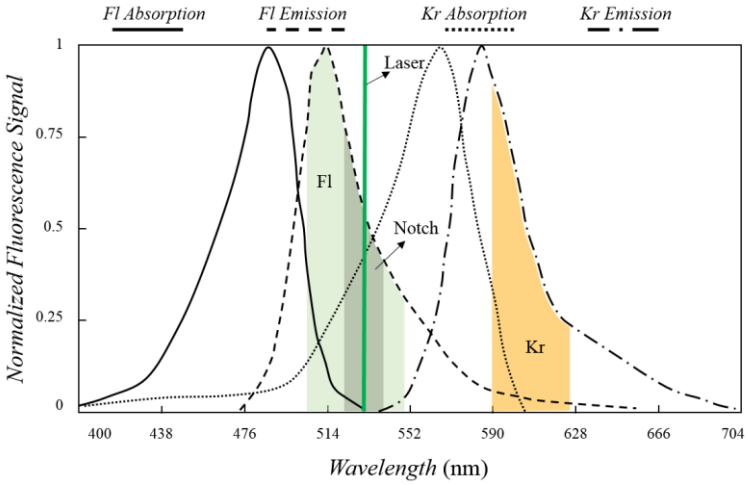

Figure 4: A plot of the absorption and emission signal variation with wavelength of Fl and Kr (*after* Behshad et al. (2010)). Different colours show the different filter wavelength range and the laser wavelength

As can be seen in Figure 5, Fl has a positive temperature sensitivity that is equal to $\sim +1.7\,\%/℃$. Kr has the temperature sensitivity of $\sim -1.6\,\%/℃$ which makes it a good pair with Fl to have a maximum temperature sensitivity under a ratiometric condition. The intensity-temperature calibration graph which shows the linear relation between the emitted signal intensity and the temperature of each fluorescent dye can be seen in Figure 5(a). The intensity-temperature calibration of the fluorescent dyes which lead to Figure 5(a) has been done using a dye calibration cell (LaVision GmbH) with the same conditions of the experiments and in the range of $15\,℃ < T < 40\,℃$. The ratiometric intensity-temperature graph, Figure 5(b), shows the temperature measurement with the maximum temperature sensitivity of $\sim 4.9\,\%/℃$.

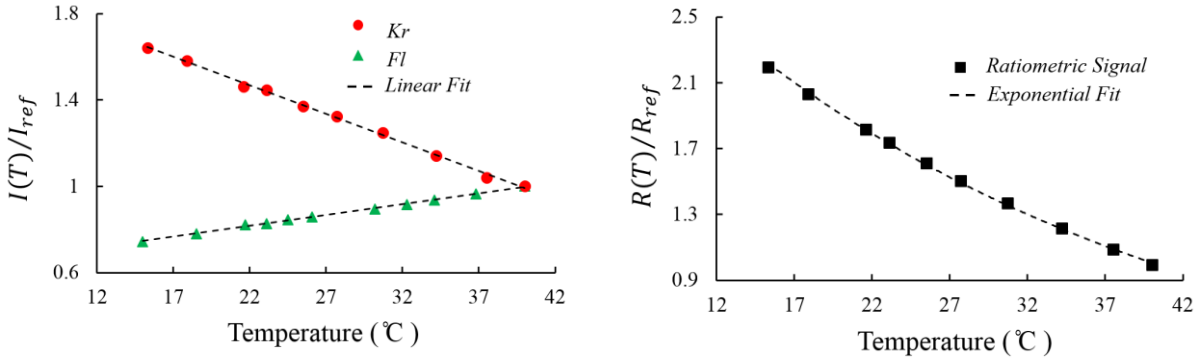

(a) (b)

Figure 5: Normalized intensity-temperature calibration graph. (a) One colour, Fl and Kr calibration, $I_{ref} = I(T = 40\ ℃)$ (b) Ratiometric intensity-temperature, $R(T) = I_{Fl}(T)/I_{Kr}(T)$

4 Time-resolved PTV

To apply PTV, hollow glass spheres with a diameter of 18 μm were used as seeding particles. A raw image of the fluid domain with seeding particles is shown in Figure 6(a). The ability of the seeding particle following the fluid flow is crucial in buoyancy-driven flows and specifically for this work because the density of flow is changing. The experiment starts from a stationary condition with no flow and the flow field was captured over the long time scale (3000 seconds) of the flow with the flow pattern became steady. Seeding particles rising velocity due to the buoyancy force can be described by:

$$V_{rise} = \frac{2\rho g D_p^2 \Delta\rho}{9\mu\rho} \tag{1}$$

which is derived from Stokes drag force of a spherical particle. Here, V_{rise} is the rising velocity, ρ is the density of the fluid, $\Delta\rho$ the density difference of the particle with the fluid, g is gravitational acceleration, D_p is the diameter of particles, and μ is the dynamic viscosity of the fluid. Considering this equation, the maximum of V_{rise} is estimated at 30 $\mu m/s$ which is deemed a significantly low value for this experiment. Also, a relaxation time of 30 minutes is implemented before the start of the experiment to ensure that the flow has achieved a stationary condition. The PIV result after the relaxation time shows that the motion of the seeding particles is negligible and it can be considered stationary.

PTV processing was applied using a commercial software (DaVis 10.0.5, LaVision GmbH) after background subtraction was applied to enhance the seeding particle intensity contrast with the background to improve their detectability, as shown in the example Figure 6(a). Particle detection criteria are defined as the seeding particles with the size in the range of 2 to 5 pixels and with an intensity higher than 20 counts. The camera frame rate is set to 30 fps, so the seeding particle's motion with the lowest velocity (at the start of the convection) to the highest velocity (developed flow) can be captured time-resolved. The depth of focus of the camera's lens is set to cover the whole 5 mm depth of the field. Calibration results show that the magnification change in the depth can be neglected. The velocity vectors obtained from the PTV processing are shown in Figure 6(b). As can be observed the velocity vectors are dispersed base on the motion and location of each detected seeding particle. To plot the velocity contour from the calculated velocity vectors, the dispersed data of the velocity is interpolated onto a structured grid with the size of 16 pixels. The results of the non-dimensional velocity contour, $V^* = V/V_{max}$ can be observed in Figure 6(c).

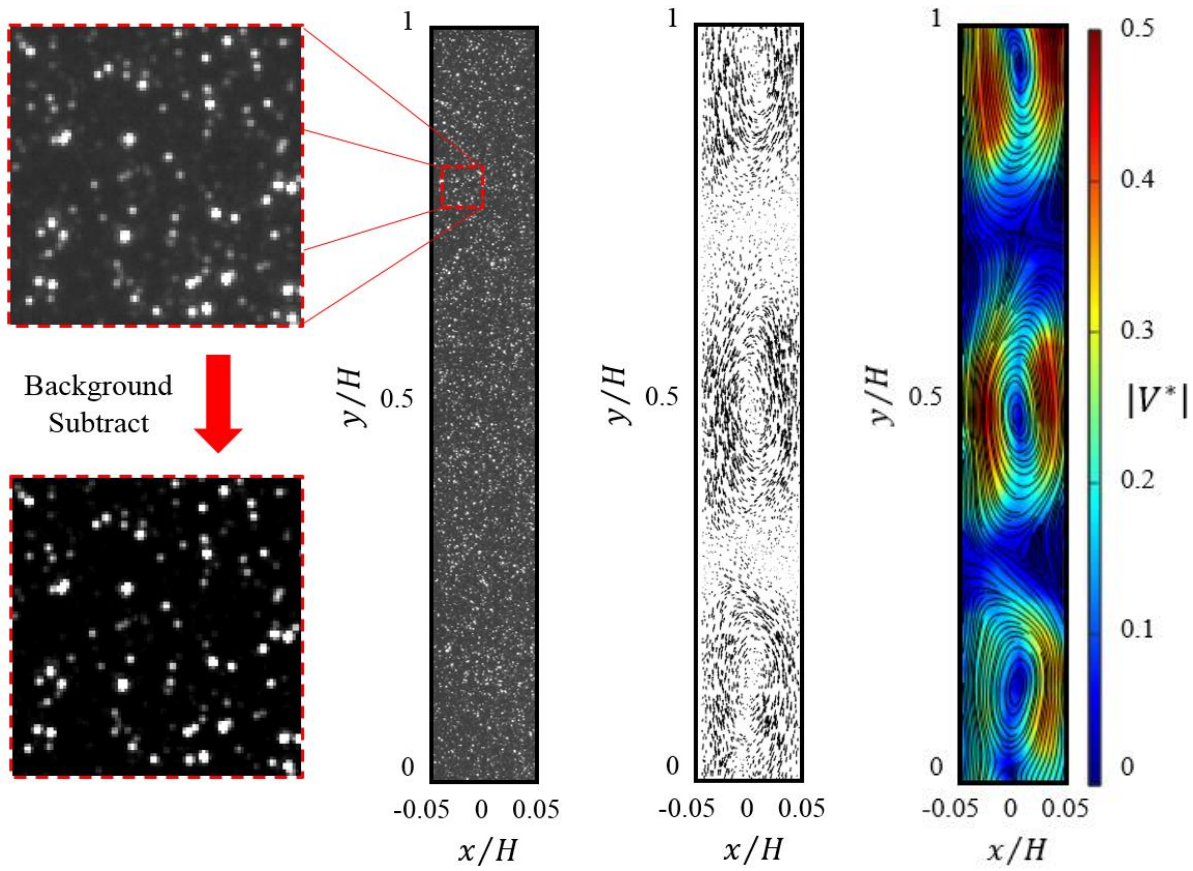

(a) (b) (c)

Figure 6: PTV procedure to calculate velocity vectors. (a) image of the field of view showing the seeding particles image before and after background subtraction, (b) velocity vectors obtained from PTV at $t = 1391$ s, (c) velocity contour and streamline obtained from interpolation on the structured grid at $t = 1391$ s

The described procedure of the velocity calculation was applied on each plane at different depths of the test cell (*z*-direction) and results in the calculation of the velocity component in *x*-*y* plane, V_x and V_y. To calculate the out-of-plane velocity component, V_z, the continuity equation:

$$\frac{\partial V_z}{\partial z} + \frac{\partial V_x}{\partial x} + \frac{\partial V_y}{\partial y} = 0 \tag{2}$$

can be applied. The first order discretized form of this equation can be expressed as:

$$\left(\frac{\partial V_x}{\partial x}\right)_{i,j,k} = \frac{V_{x_{i+1,j,k}} - V_{x_{i,j,k}}}{\Delta x} \tag{3}$$

$$\left(\frac{\partial V_y}{\partial y}\right)_{i,j,k} = \frac{V_{y_{i,j+1,k}} - V_{y_{i,j,k}}}{\Delta y} \tag{4}$$

$$\left(\frac{\partial V_z}{\partial z}\right)_{i,j,k} = \frac{V_{z_{i,j,k+1}} - V_{z_{i,j,k}}}{\Delta z} \tag{5}$$

Considering the nonslip boundary condition in which $V_x = V_y = V_z = 0$, equation(3) to (5) can be solved implicitly on the structured grid for all the 50 planes captured by scanning the flow domain. In these

equations, i, j, and k represent the discretization in x, y, and z direction with Δx, Δy, and Δz distance. This calculation results in obtaining the out-of-plane velocity distribution for the whole fluid domain.

4 Results

Temperature measurement, $T^* = (2T)/((T_{max} + T_{min}))$, for the onset of convection are shown in Figure 7(a) to (d). In this case, the temperature of the bottom and top surfaces are equal to 45 ℃ and 5 ℃ respectively. Before the onset of convection, the fluid is at the stationary condition and the temperature of the fluid is constant and equal to $T^* = -0.35$. As can be observed in the figure, the convection starts by rising and falling a hot and cold plume respectively. Figure 7(c) shows the first interaction between the two plumes which leads to temperature moderation of each part of the flow (hot and cold) and formation of two columns of the flow, a hot column at the right-hand side and a cold column at the left-hand side shown in Figure 7(d). The result of the temperature distribution shows a significant temperature variation during the 3000 seconds of the experiment for this regime, $Ra = 5.5 \times 10^8$. The temperature distribution after 1391 seconds is shown in Figure 7(e). Despite of Figure 7(c) which has two thermal zones, in this figure the temperature distribution is more complex.

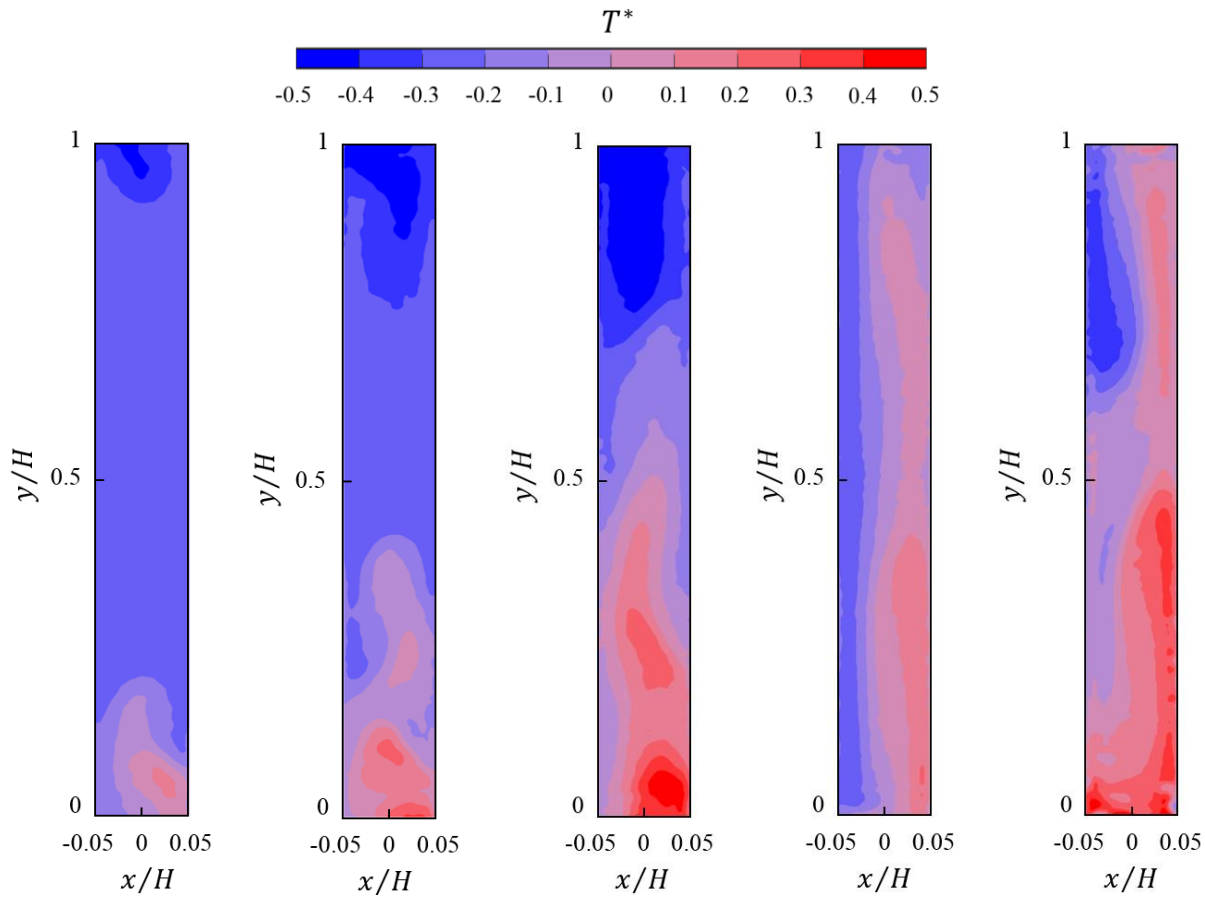

Figure 7: Temperature variation at the different times (a) $t = 8$ s, (b) $t = 19$ s, (c) $t = 34$ s, (d) $t = 54$ s, (e) $t = 1391$ s

For the same experimental conditions, the results of the PTV, $V^* = (2V)/((V_{max} + V_{min}))$ is shown in Figure 8(a) to (d). Though the results are taken in two separate experiments, the velocity vectors describe the same phenomenon at the onset with a small time difference visualized with the temperature distribution.

From Figure 8(a) and (b), the rise and fall of the hot and cold plumes can be observed. Figure 8(c) shows the first interaction between these plumes and Figure 8(d) shows the flow structure in which two thermal zones were described, Figure 7(d). Comparing Figure 7(d) and Figure 8(d) it can be observed that the hot zone is the rising zone and the cold zone is the falling zone.

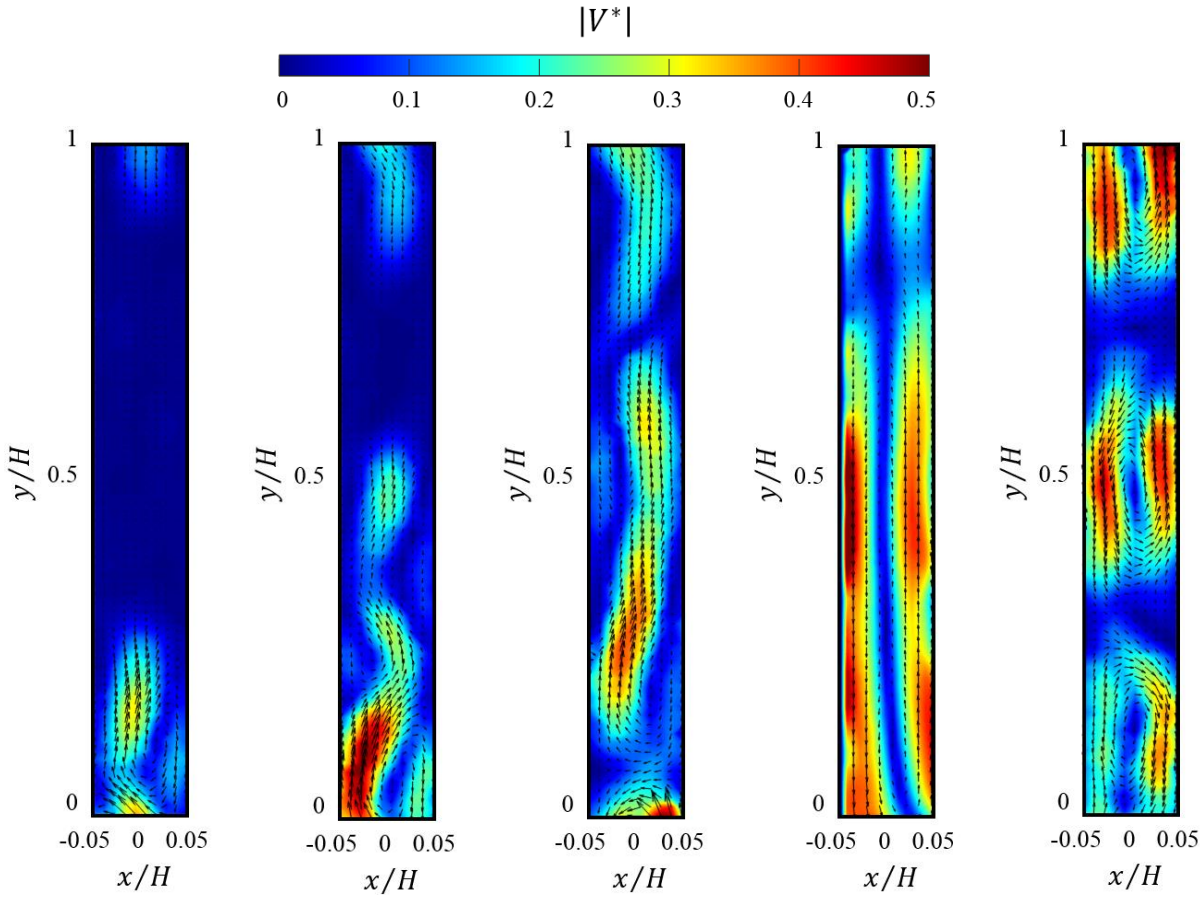

Figure 8: Velocity variation at the different times (a) $t = 8$ s, (b) $t = 20$ s, (c) $t = 36$ s, (d) $t = 64$ s, (e) $t = 1391$ s

The results of the velocity visualization during onset of the flow shows that this regime is unsteady. The velocity of the flow field at $t = 1391$ s, is shown in Figure 8(e) which three LSCs can be observed. Though the time of this PTV result is same as what was shown for the temperature in Figure 7(d), the flow topology is much more complex rather at onset, which makes it more difficult to compare the thermal plume dynamics with the velocity. This observation shows the importance of collecting simultaneous measurements of the temperature and velocity to fully characterize the flow.

As an example of the in-plane flow structure evaluation in different elevenation in the z-direction, is shown in Figure 9 for five different depths of the test cell. This shows the evaluation of the flow structure from $z^* = -0.041$ to $z^* = 0.041$ where $z^* = z/H$. The series of 50 planes from $z^* = -0.05$ to $z^* = 0.05$ is going to use to calculate out-of-plane velocity component.

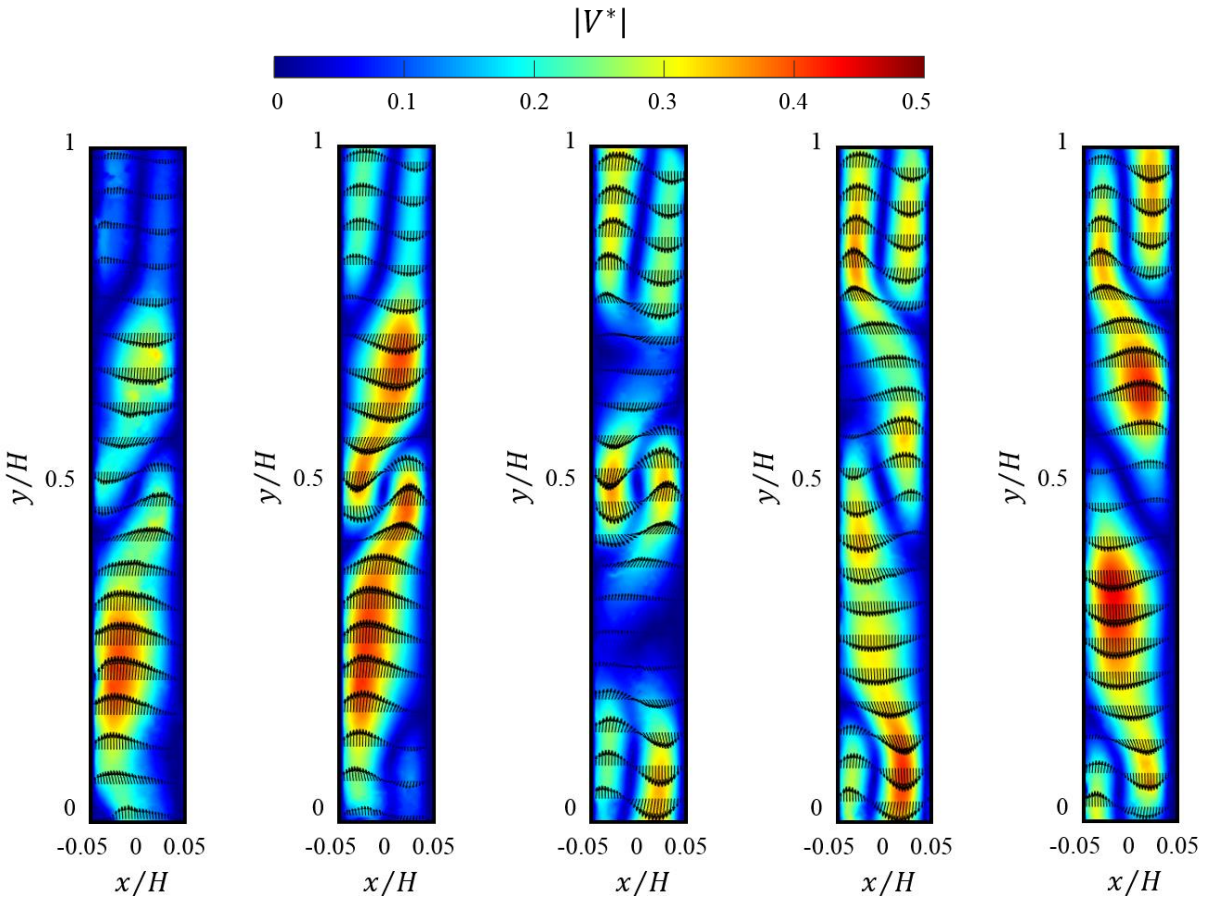

Figure 9: Velocity distribution on the different planes (in *z*-direction). (a) $z^* = -0.041$, (b) $z^* = -0.033$, $z^* = 0$, $z^* = 0.033$, $z^* = 0.041$

Conclusion

The methodology of applying time-resolved 2-D PTV and two-colour PLIF on studying the RBC in a highly slender cell with an aspect ratio of 0.1 was discussed. For time-resolved two-colour PLIF, The procedure of the fluorescent dye selection and calibration were discussed. Furthermore, the result of the temperature measurement for different times were shown. Regarding the velocity measurement, implementation of a scanning system to apply 2-D PTV at different depths of the flow domain was shown with presenting the results of the different depths. All the presented work was a part of a procedure for applying these two techniques simultaneously in the future.

Acknowledgement

The authors acknowledge financial support from Future Energy Systems (FES) and the Natural Sciences and Engineering Research Council (NSERC) of Canada.

References

B. Adrian (2013) *Convection heat transfer*. John Wiley and Sons, Inc.

Jeffrey A Sutton, Brian T Fisher, and James W Fleming. (2008) A laser-induced fluorescence measurement for aqueous fluid flows with improved temperature sensitivity. *Experiments in Fluids* 45:869–881

Behshad, M, Shafii, Chee, L Lum, and Manoochehr M Koochesfahani (2010) In situ lif temperature measurements in aqueous ammonium chloride solution during uni-directional solidification. *Experiments in Fluids* 48:651–662

Bown, M. R., J. M. MacInnes, and R. W.K. Allen. (2007) Three-component micro-piv using the continuity equation and a comparison of the performance with that of stereoscopic measurements. *Experiments in Fluids* 42: 197–205

Couston, Louis Alexandre, Daniel Lecoanet, Benjamin Favier, and Michael Le Bars. (2019) Shape and size of large-scale vortices: a universal fluid pattern in geophysical fluid dynamics. *Physical Review Research* 2: 23143

Fujisawa, N., S. Funatani, and N. Katoh. (2005) Scanning liquid-crystal thermometry and stereo velocimetry for simultaneous three-dimensional measurement of temperature and velocity field in a turbulent Rayleigh-Bernard convection. *Experiments in Fluids* 38: 291–303

Kazemi, Mohammad Amin, Janet A W Elliott, and David S Nobes. (2016) Determination of the three components of velocity in an evaporating liquid from scanning PIV. in *18th International Symposium on Applications of Laser Techniques to Fluid Mechanics*.

Kim, H. J., and K. D. Kihm. (2001) Application of a two-color laser induced fluorescence (LIF) technique for temperature mapping. in *American Society of Mechanical Engineers, Heat Transfer Division*

Lohse, Detlef, and Ke Qing Xia. (2010) Small-scale properties of turbulent Rayleigh-Benard convection. *Annual Review of Fluid Mechanics* 42: 335–64

Miroshnichenko, I. V., and M. A. Sheremet. (2018) Turbulent natural convection heat transfer in rectangular enclosures using experimental and numerical approaches: a review. *Renewable and Sustainable Energy Reviews* 82: 40–59

Raffel, Markus, Willert, Christian E., Scarano, Fulvio, Kähler, Christian J., Wereley, Steve T., Kompenhans, Jürgen (2018) *Particle image velocimetry: a practical guide.* Springer

Sakakibara, J, and R J Adrian. (1999) Whole field measurement of temperature in water using two-color laser induced fluorescence. *Experiments in Fluids* 26: 7-15

Song, Xudong, and David S. Nobes. (2011) Experimental investigation of evaporation-induced convection in water using laser based measurement techniques. *Experimental Thermal and Fluid Science* 35: 910–19.

Lukas Zwirner, Andreas Tilgner, and Olga Shishkina. (2020) Elliptical instability and multiple-roll flow modes of the large-scale circulation in confined turbulent Rayleigh-Benard convection. *Physical Review Letters* 125, 05402